Research Article Vol. 33, No. 18 / 8 Sep 2025 / Optics Express 38984

Optics EXPRESS

Perturbative Fourier ptychographic microscopy for fast quantitative phase imaging

MARTIN ZACH,[1,2,†] KUAN-CHEN SHEN,[1,†] RUIMING CAO,[3]
MICHAEL UNSER,[1] LAURA WALLER,[3] AND JONATHAN DONG[1,*]

[1] Biomedical Imaging Group, École Polytechnique Fédérale de Lausanne, 1015 Lausanne, Switzerland
[2] Center for Biomedical Imaging, 1015 Lausanne, Switzerland
[3] Department of Electrical Engineering and Computer Sciences, University of California, Berkeley, CA 94709, USA
[†] These authors contributed equally.
[*] jonathan.dong@epfl.ch

Abstract: In computational phase imaging with a microscope equipped with an array of light emitting diodes as the illumination unit, conventional Fourier ptychographic microscopy achieves high resolution and wide-field reconstructions but is constrained by a lengthy acquisition time. Conversely, differential phase contrast (DPC) offers fast imaging but is limited in resolution. Here, we introduce perturbative Fourier ptychographic microscopy (pFPM). pFPM is an extension of DPC that incorporates dark-field illumination to enable fast, high-resolution, wide-field quantitative phase imaging with few measurements. We interpret DPC as the initial iteration of a Gauss-Newton algorithm with quadratic regularization and generalize it to multiple iterations and more sophisticated regularizers. This broader framework is not restricted to bright-field measurements and allows us to overcome resolution limitations of DPC. We develop tailored dark-field illumination patterns with ring shapes, that align with the perturbative interpretation and lead to an improvement in the quality of reconstruction with respect to other common illumination schemes. Consequently, our methodology combines an enhanced phase reconstruction algorithm with a specialized illumination strategy and offers significant advantages in both imaging speed and resolution.

1. Introduction

Phase imaging, rooted in the development of the Zernike phase-contrast microscope [1], has become an essential technique for the imaging of unstained biological specimens [2]. Techniques such as holography [3] or Fourier ptychography [4] retrieve quantitative phase maps via computational algorithms and have found use in many areas of biomedical research, such as histopathology or developmental biology [2,5,6].

In recent years, the light-emitting diode (LED)-array microscope has emerged as a versatile tool for computational phase imaging [7–9]. In such a system, users capture measurements under different illumination angles using a programmable illumination unit. In particular, LEDs positioned within the disc defined by the microscope's numerical aperture (NA) provide bright-field illumination, while those that lie outside this disc deliver dark-field illumination, as sketched in Fig. 1. Importantly, the illumination patterns are tightly interlinked with the reconstruction algorithm. Indeed, for bright-field-only illumination, a linear model of the setup is a sufficient approximation when unscattered light is dominant, whereas dark-field illumination necessitates nonlinear recovery algorithms.

The most popular phase imaging methods using LED-array microscopes are on the two ends of the speed-resolution tradeoff. On the one hand, Fourier ptychographic microscopy (FPM)

#560811 https://doi.org/10.1364/OE.560811
Journal © 2025 Received 27 Feb 2025; revised 3 Aug 2025; accepted 16 Aug 2025; published 5 Sep 2025

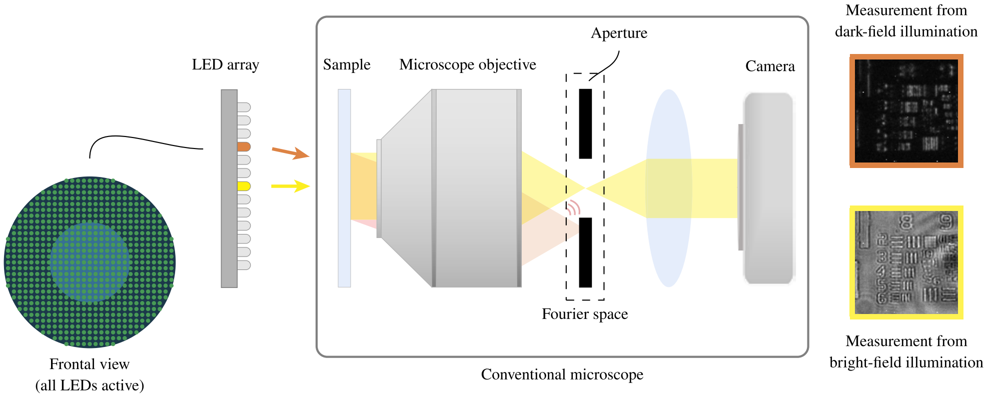

Fig. 1. LED microscope. A programmable LED array plays the role of the illumination unit. In the frontal view of the LED array on the far left, the inner disk is the bright-field region and the dots are the LEDs. The propagation of the illumination from an LED in the bright-field and the dark-field mode is shown next. Corresponding measurements of the USAF-1951 phantom are shown on the right.

[4,10,11] entails the acquisition of one measurement per (bright-field and dark-field) LED, typically in the range of hundreds of measurements. The reconstruction of the high-resolution, wide field-of-view images is done with nonlinear optimization algorithms, typically gradient descent [12,13]. On the other hand, DPC [9,14–16] entails the acquisition of two measurements from asymmetric bright-field illumination patterns. There, the weak-object approximation enables one to reconstruct the phase by solving a linear system. However, the linear model only considers bright-field illumination, which limits the achievable resolution.

To image living specimens with acceptable speed, it is essential to minimize the number of required measurements per reconstruction. multiplexed Fourier ptychographic microscopy (mFPM) [8] addresses this by the simultaneous use of multiple LEDs, thus merging the speed of DPC with the high resolution of FPM. However, the nonlinear optimization becomes increasingly difficult as the number of measurements is reduced, while the optimal design of illumination patterns remains an open problem. These limitations can partly be addressed by the learning of illumination patterns [17] or the fine tuning of parameters of a reconstruction algorithm [18,19] which both improve the quality of mFPM reconstruction. However, the learned methods tend to be opaque, hard to interpret, and highly tailored toward specific imaging conditions.

Other approaches enabled single-shot phase imaging thanks to the introduction of a microlens array [20], a diffraction grating [21] or color [22] and polarization [23,24] multiplexing. These methods have the drawback of relying on new optical elements, while the simplicity of the LED array microscope stems in its simplicity and versatility.

In this work, we introduce pFPM for high-resolution phase imaging with few measurements. We revisit both the reconstruction algorithm and the acquisition strategy from an optimization perspective to tackle the speed-resolution tradeoff. First, we interpret the DPC reconstruction process that is based on the weak-object linearization as the initial iteration of a Gauss-Newton algorithm. We then generalize this into a proximal Gauss-Newton framework that accounts for dark-field illumination, with more sophisticated regularization to improve the robustness of phase retrieval. Second, we design dark-field illumination patterns with ring shapes that “extend” reconstructed frequencies into the dark-field region, thereby enhancing resolution. We demonstrate the effectiveness of the proposed approach through numerical simulations and experimental results.

In summary, our methodology extends the DPC linearization to dark-field images using ring dark-field illumination patterns. This approach improves the achievable resolution at little expense in imaging speed through the addition of few illumination patterns that are tailored to the linearization that is encountered in the optimization algorithm. In addition, the proximal Gauss-Newton algorithm provides a flexible framework for the consideration of regularizers with superior noise-suppression properties than those of the standard L^2 regularizer.

2. Background

2.1. LED-array microscope

The resolution of a classic microscope is determined by the NA ν_{obj} of its objective, which sets a limit on the largest acquired spatial frequencies. To bypass this limit, in an LED-array microscope the conventional illumination unit is replaced by a programmable LED array. By illuminating the sample with tilted plane waves, the system gets access to a broader range of spatial frequencies than would be possible under normal incidence.

The illumination NA ν_{ill} is defined as the sine of the largest tilt angle. When combined with the numerical aperture of the objective, the achievable resolution is defined by the spatial frequency cutoff $(\nu_{\mathrm{obj}} + \nu_{\mathrm{ill}})/\lambda$, where λ is the average illumination wavelength. Such setups typically use a low-NA objective to maximize the field-of-view while achieving high resolution in reason of a large illumination NA. LEDs are categorized based on their position relative to the aperture of the microscope: Bright-field LEDs lie within the cone defined by ν_{obj}, thereby allowing unscattered light to pass through the objective and to yield high-intensity measurements that contain low-frequency information. In contrast, dark-field LEDs lie outside this cone and generate dim measurements from scattered light that contain high-frequency information.

The model of an LED-array microscope is sketched in Fig. 1. Formally, the illumination of the transmission function $o : \mathbb{R}^2 \to \mathbb{C}$ of the object with the nth LED results in the intensity measurement

$$y_n(\mathbf{r}) = \left|\mathcal{F}^{-1}\{p\mathcal{F}\{o(\,\cdot\,)\exp(\mathrm{j}\langle \mathbf{k}_n, \cdot\,\rangle)\}\}(\mathbf{r})\right|^2, \tag{1}$$

where the LED index n ranges from 1 to the total number of LEDs in the programmable illumination unit, denoted N. The wave vector $\mathbf{k}_n \in \mathbb{R}^2$ is associated to the nth LED and corresponds to the angle of illumination. We assume that the microscope is aberration-free and, consequently, characterize it by a pupil function p that is equal to 1 inside the circular aperture and 0 outside. The symbols $\mathcal{F}$ and $\mathcal{F}^{-1}$ denote the two-dimensional Fourier transform and its inverse, respectively, and $|\cdot|$ is the modulus. We later denote by $\mathcal{A}_n\{o\} = \mathcal{F}^{-1}\{p\mathcal{F}\{o(\,\cdot\,)\exp(\mathrm{j}\langle \mathbf{k}_n, \cdot\,\rangle)\}\}$ the field in the camera sensor plane resulting from illumination with the nth LED.

The intensity measurements obtained with several LEDs being active are incoherently superimposed. Formally, the set $\mathcal{L}_m \subseteq \{1, 2, \ldots, N\}$ of active LEDs, termed an illumination pattern, results in the intensity measurement

$$Y_m(\mathbf{r}) = \sum_{n \in \mathcal{L}_m} y_n(\mathbf{r}). \tag{2}$$

The system then ranges through $m = 1, 2, \ldots, M$ distinct illumination patterns to acquire M measurements. Letting $Y = (Y_1, Y_2, \ldots, Y_M)$, we state the relationship between the transmission function o and the measurements as

$$Y = G(o), \tag{3}$$

where G summarizes the nonlinear acquisition process from the M illumination patterns according to

$$G(o) = \left(\sum_{n \in \mathcal{L}_1} \left|\mathcal{A}_n\{o\}^2, \ldots, \sum_{n \in \mathcal{L}_M} \mathcal{A}_n\{o\}\right|^2\right). \tag{4}$$

The challenge in this setup is to find M illumination patterns and an accompanying algorithm that enables the efficient recovery of the complex-valued transmission function o from the measurements Y. Crucially, M needs to be small to achieve fast imaging and sufficiently large to ensure the robustness of the solution to the nonlinear inverse problem. In the following sections, we give an overview of proposed illumination patterns and reconstruction algorithms.

2.2. Conventional Fourier ptychographic microscopy

Conventional FPM dates back to the work of Zheng, Horstmeyer, and Yang [4], where single-LED measurements are employed as illustrated in Fig. 2(a). A variety of algorithms address the recovery of the transmission function o from the intensity measurements; in the original work, the authors stitch the Fourier space of the reconstruction to be consistent with the intensity measurements in an alternated-projection manner. Subsequent works optimize the nonlinear least-squares problem associated with (3) with gradient-based methods with various acceleration strategies [12] or a coded sensor to improve low-frequency transfer [25].

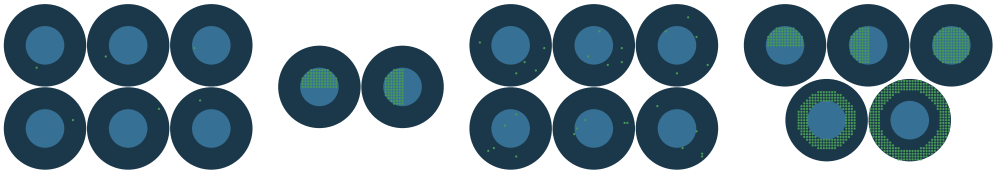
(a) FPM (b) DPC (c) mFPM (d) pFPM

Fig. 2. Illumination patterns of different methods. The inner disk indicates the bright-field region while the dots depict active LEDs. The proposed method (pFPM) combines bright-field illumination patterns with dark-field illumination rings.

In the conventional setup, the phase reconstruction requires large overlap ratios of the passband of adjacent LEDs between 0.4 and 0.7 [4,26]. This necessitates a tight LED array and, consequently, many (typically a few hundred) measurements. This leads to long acquisition time and limits the temporal resolution of conventional FPM, making it inadequate for fast time-lapse imaging.

2.3. Multiplexed Fourier ptychographic microscopy

To shorten acquisition time, the authors of [8] propose to illuminate the object with multiple, randomly chosen LEDs, thereby reducing the number of measurements needed to achieve results comparable to conventional FPM. Moreover, the increased light throughput from multiple LEDs lowers exposure requirements and therefore enables the imaging of dynamic objects at high frame rates. Formally, the illumination patterns, sketched in Fig. 2(c), are random subsets of $\{1, 2, \ldots, N\}$ of size r (typically in the single digits), and M is chosen as N/r.

Like in conventional FPM, researchers often use gradient-based nonlinear optimization algorithms to recover the transmission function o from the multiplexed intensity measurements $Y_1, Y_2, \ldots, Y_M$ [8,9]. More recently, researchers have leveraged machine-learning-based methods to improve the quality of the reconstruction [18,27,28].

The recourse for as few as possible illumination patterns is paramount to enable the imaging of dynamic objects. Following the introduction of random patterns in [8], the authors of [29] advocate for a separation of bright-field and dark-field patterns. They combine the classic DPC bright-field patterns with random dark-field patterns, ultimately resulting in $M = 21$ measurements. Xue et al. [18] proposed the use of five illumination patterns—two bright-field patterns inspired by DPC plus three annular sectors in the dark-field—within a data-driven reconstruction framework. Instead of fixing them a-priori, Kellmann et al. [30] learn illumination patterns in a data-driven framework and demonstrate successful reconstructions with a single-digit number of illumination patterns. The approaches in [18] and [30] ultimately result in reconstruction algorithms that are difficult to interpret and tailored to highly specific imaging conditions or samples.

2.4. Differential phase contrast

Instead of relying on nonlinear optimization, DPC linearizes the recovery problem around a suitable initial guess and uses direct inversion under suitable illumination patterns to recover an estimation of the transmission function. Nowadays, DPC is used in the context of linearized methods with asymmetric illumination patterns, as we use it here. Originally, the name stems from the computation of the "differential" between intensity measurements from two mirrored asymmetric illumination patterns, canceling any influence of absorption [9]. For the derivation of the direct inversion, it is convenient to parametrize the transmission function as

$$o = 1 + \mathrm{j}\phi - \mu, \tag{5}$$

where $\phi, \mu : \mathbb{R}^2 \to \mathbb{R}$ are real-valued functions that correspond to phase and absorption, respectively, of the transmission function. This refers to the linearization of $(\phi, \mu) \mapsto \exp\big(\mathrm{j}\phi(\,\cdot\,) - \mu(\,\cdot\,)\big)$ around $(0, 0)$. This additional linearization can be avoided by the direct parametrization of o defined in (5). The fundamental assumption in DPC is that the object is weak in the sense that both μ and ϕ are small.

Under this approximation, the Fourier transform of the intensity measurement that result from the illumination with the nth LED is related to ϕ and μ via

$$\mathcal{F}\{y_n\} = |p(\mathbf{k}_n)|^2\,\delta + h_n^{\mathrm{abs}}\mathcal{F}\{\mu\} + h_n^{\mathrm{ph}}\mathcal{F}\{\phi\}, \tag{6}$$

where

$$h_n^{\mathrm{ph}} = \mathrm{j}\big(\overline{p}(\mathbf{k}_n)p(\mathbf{k}_n + \,\cdot\,) - p(\mathbf{k}_n)\overline{p}(\mathbf{k}_n - \,\cdot\,)\big) \tag{7}$$

and

$$h_n^{\mathrm{abs}} = -\big(\overline{p}(\mathbf{k}_n)p(\mathbf{k}_n + \,\cdot\,) + p(\mathbf{k}_n)\overline{p}(\mathbf{k}_n - \,\cdot\,)\big) \tag{8}$$

are the phase- and absorption-transfer function, respectively, where the overbar denotes conjugation and δ the Dirac distribution. A derivation is provided in Section 1 of Supplement 1. Due to the superposition of multiplexed measurements in (2), they can be accounted for by a summation of the transfer functions for the LEDs of each illumination pattern: $H_m^{\mathrm{ph}} = \sum_{n \in \mathcal{L}_m} h_n^{\mathrm{ph}}$. A common simplification [30] (e.g., in the context of unstained biological samples) involves a phase-only sample, as defined by $\mu = 0$ in (5).

The presence of noise in the measurements necessitates one to formulate the recovery as a regularized least-squares problem. For instance, L^2 regularization is used in [9,16,23]. Thus, the recovery is posed as the problem

$$\operatorname{argmin}_{\phi}\left(\sum_{\mathrm{m}=1}^{\mathrm{M}} \tfrac{1}{2} \parallel \mathcal{F}^{-1}\{\mathrm{H}_{\mathrm{m}}^{\mathrm{ph}}\mathcal{F}\{\phi\}\} - \mathrm{Y}_{\mathrm{m}} \parallel_2^2 + \tfrac{\alpha}{2} \parallel \phi \parallel_2^2\right), \tag{9}$$

whose solution is

$$\mathcal{F}^{-1}\left\{\frac{\sum_{m=1}^{M} \overline{H_m^{\mathrm{ph}}}\mathcal{F}\{Y_m\}}{\sum_{m=1}^{M} \left|H_m^{\mathrm{ph}}\right|^2 + \alpha}\right\}. \tag{10}$$

Regarding the design of the illumination patterns, the antisymmetric structure of the phase-transfer function in (7) suggests the use of antisymmetric bright-field illumination patterns. To get full coverage of the spectrum, DPC is usually done with $M = 2$ illumination patterns, where one is rotated by $\frac{\pi}{2}$ [9, Fig. 3], [30, Fig. 3(a)], see Fig. 2(b).

In summary, DPC linearizes the acquisition operator around a suitable initial guess and subsequently estimates the transmission function under some regularization. This approach is fast and robust, but the linear model requires the weak-object approximation. Consequently, it is only applicable to measurements from bright-field illumination and limits the achievable resolution improvement to a factor of two.

3. Method

In this section, we introduce a perturbative formalism to exploit good initial estimates and refine them. Computationally, we show that the single-shot linearization of DPC can be extended to an iterative regularized Gauss-Newton algorithm. Experimentally, we introduce ring illuminations that take full advantage of this perturbative interpretation to refine the reconstruction using dark-field LEDs.

3.1. *Perturbative FPM algorithm*

We first revisit the weak-object approximation of DPC in our general perturbative framework. The nonlinear measurement process (3) is well-approximated by the linearization around $(\mu, \phi) = (0, 0)$ or, equivalently, $o = 1$ as

$$Y \approx G(1) + G'(1)(o - 1), \tag{11}$$

where G' is the Fréchet derivative of G, defined at an arbitrary point o^k by

$$G'(o^k) : o \mapsto \left(\sum_{n \in \mathcal{L}_1} 2\Re\left(\overline{\mathcal{A}_n\{o^k\}}\mathcal{A}_n\{o\}\right), \ldots, \sum_{n \in \mathcal{L}_M} 2\Re\left(\overline{\mathcal{A}_n\{o^k\}}\mathcal{A}_n\{o\}\right) \right). \tag{12}$$

We identify DPC as the initial iteration of the iterative procedure

$$o_{k+1} = \mathrm{argmin}_{\mathrm{o}} \left(\tfrac{1}{2} \parallel \mathrm{G}(\mathrm{o}_\mathrm{k}) + \mathrm{G}'(\mathrm{o}_\mathrm{k})(\mathrm{o} - \mathrm{o}_\mathrm{k}) - \mathrm{Y} \parallel_2^2 + \alpha \mathrm{R}(\mathrm{o}) \right) \tag{13}$$

under the choice $R(o) = \frac{1}{2} \parallel o \parallel_2^2$ and starting with $o_0 = 1$ as the initial guess. This equivalence is rigorously derived in Section 2 of Supplement 1. This reformulates DPC as a particular case of perturbative updates based on initial estimates. For example, iterating (13) corresponds to using the previous estimate as a new initial guess, enabling further refinements of the estimate beyond the weak-object approximation. Moreover, our generalization to more iterations enables the reconstruction of image features from dark-field measurements, as subsequent iterations do not rely on the weak-object approximation.

We recognize (13) as the proximal Gauss-Newton algorithm [31] and generalize DPC to more iterations and more sophisticated regularizers with superior noise-suppression properties. In this paper, we demonstrate the benefit of this generalization by comparing total variation (TV) regularization to the previously used L^2 regularization. The framework is not restricted to this; in particular, data-driven regularizers could also be employed. Indeed, we believe that any phase-retrieval method can benefit from the stronger noise suppression properties of the variational penalties that can be used in the proximal Gauss-Newton framework. The iteration rule described in (13) is valid for various different choices of G, which includes conventional FPM and mFPM with arbitrary multiplexing patterns.

In particular, the initial guess $o_0 = 1$ enables the explicit computation of the phase transfer function with the standard techniques given in 2.4 (see, e.g., [9, Fig. 2] for the phase transfer function of the standard DPC patterns). Thus, o_1 is solely determined by the bright-field LEDs and the cost of its computation is equivalent to the cost of computing the DPC reconstruction (assuming L^2 regularization). Subsequent iterations do not rely on the weak object approximation and, consequently, can use dark-field information without any special handling in the optimization; iterates gracefully shift from a reconstruction based purely on information from bright-field LEDs to one that is also consistent with the dark-field measurements.

3.2. Perturbative FPM patterns

In this section, we detail an acquisition strategy that exploits the combination of DPC-type patterns with darkfield rings to enable fast high-resolution imaging with few illumination patterns that are tailored towards the perturbative approach. In the bright-field, we exploit the antisymmetric bright-field illumination patterns of DPC that enable the accurate recovery of the frequencies of the transmission function up to $k_{\mathrm{BF}} = 2\nu_{\mathrm{obj}}/\lambda$ when the object is weak, similar to [29]. In the dark-field, we build on previous works [17,32] which show that dark-field illumination patterns need not be antisymmetric—indeed, reconstruction quality increases when dark-field illumination patterns are actually symmetric, disjoint, and clustered. Consequently, we partition the dark-field LEDs into rings, as shown in Fig. 2(d), each forming an illumination pattern, to allow for the recovery of higher frequencies from dark-field measurements after the DPC solution. The inner ring "pushes" the recovered frequencies slightly above the bright-field region in Fourier space, and the outer ring further enhanced the recovered frequencies into the dark-field region.

Each ring extends the region of recovered frequencies. Although the number of rings is tunable and balances acquisition time with reconstruction quality, our simulations and experiments show excellent results with only two rings and diminishing returns with more than two rings, when doubling the bright-field illumination NA. Thus, we recommend the use of two dark-field measurements to double the illumination NA and significantly enhance the quality of the reconstruction at the least expense in imaging speed.

While we do not claim that these dark-field illumination patterns are rigorously optimal, our results demonstrate that they yield superior reconstruction performance compared to previously proposed patterns. Furthermore, their structure aligns well with our perturbative strategy: leveraging and refining the DPC reconstruction in the bright-field region to provide a good initial estimate, which is then used to recover information in the dark-field region.

4. Results

In this section, we verify experimentally the proposed reconstruction algorithm and illumination patterns. In the sequel, DPC refers to the direct phase inversion (10) while algorithms with the suffix pFPM use multiple proximal Gauss-Newton iterations. For the actual practice, we discourage the use of those methods that we have marked with an asterisk (*), even though we report them because they provide additional insight. BF-pFPM* uses only the two classic DPC illumination patterns, BF-pFPM takes advantage of one additional bright-field illumination pattern, and DF-pFPM of two additional dark-field illumination patterns. For the computational experiments, we use L^2 regularization to match the DPC reconstruction. For the practical experiments, we use TV regularization to benefit from its superior noise-suppression properties. Details such as the number of iterations and the choice of stepsizes are given in Section 4 of Supplement 1.

The results from simulated and experimental data are acquired after a standard discretization of the system on the regular Cartesian grid. The discretization of the transmission function, the intensity measurements, and all relevant operators, is detailed in Section 3 of Supplement 1. We also provide online the code and data to reproduce our results [34].

4.1. Simulation

We simulate measurements from a microscope equipped with a 10× objective with numerical aperture $\nu_{\mathrm{obj}} = 0.2$ and a camera pixel size of 5.5 μm. An LED array consisting of (29×29) LEDs with wavelength 514 nm on a regular grid spaced by 4 mm is positioned 67.5 mm from a phase-only object with phase values in $[-0.5rad, 0.5rad]$, as derived from the cameraman image provided by skimage.data (see the details in Section 6 of Supplement 1). LEDs up to $\nu_{\mathrm{ill}} = 2\nu_{\mathrm{obj}} = 0.4$ are illuminated, which results in a total NA of $\nu_{\mathrm{obj}} + \nu_{\mathrm{ill}} = 0.6$.

We show the reconstructions from the different methods in Fig. 3. To facilitate interpretation, we also show the relative Fourier error maps defined by

$$|\mathbf{F}\angle(\mathbf{x}^*) - \mathbf{F}\angle(\hat{\mathbf{x}})/\mathbf{F}\angle(\mathbf{x}^*)| \tag{14}$$

clamped to a maximum of 1, where $\mathbf{F}$ is the two-dimensional discrete Fourier transform, $\mathbf{x}^*$ the reference object, $\hat{\mathbf{x}}$ the reconstruction, and $\angle$ the element-wise argument of a complex vector. The relative Fourier error map of BF-pFPM*, shown in Fig. 3(b), demonstrates that multiple Gauss-Newton iterations enable the exact recovery of most frequencies in the passband. Meanwhile, the DPC reconstruction shown in Fig. 3(a) suffers from the errors made in the linearization that corresponds to the weak-object approximation. However, since pFPM optimizes the complex vector (as opposed to only the phase), ambiguities manifest themselves as large errors along the direction in which the illumination pattern are mutually symmetric. This is seen in the DPC Eq. (6) as the goal is to recover $\mathcal{F}\{\mu\}$ and $\mathcal{F}\{\phi\}$ using the multiplexed measurements $\mathcal{F}\{Y_m\}$ for $m = 1, \dots, M$. When $M = 2$, this 2×2 linear system is in general invertible but for a few elements on a diagonal. These errors lead to oriented streaking artifacts in the reconstruction. The addition of one measurement from a full bright-field illumination mitigates this issue and the algorithm is able to recover frequencies up to k_{BF} completely. Finally, with the addition of measurements from two dark-field illumination patterns with rings spanning $[1, 1.5]\nu_{\mathrm{obj}}$ and $[1.5, 2]\nu_{\mathrm{obj}}$, high frequencies are recovered well. The qualitative results are supported by the signal-to-noise ratio (SNR) and root-mean-squared error (RMSE) disclosed in Fig. 3, with

$$\mathrm{SNR} = 10 \log_{10} \frac{\| \angle(\mathbf{x}^*) \|^2}{\| \angle(\hat{\mathbf{x}}) - \angle(\mathbf{x}^*) \|^2} \tag{15}$$

and

$$\mathrm{RMSE} = \|\angle(\hat{\mathbf{x}}) - \angle(\mathbf{x}^*) \| / \sqrt{N}. \tag{16}$$

The comparison with a reference method (the FPM reconstruction obtained from $M = 672$ measurements resulting from the illumination of all individual LEDs up to $2\nu_{\mathrm{obj}}$) shows that our method can recover a significant amount of high-detail information at minimal expense in imaging speed.

The proposed annular illumination patterns are inspired by the perturbative principle. To validate their design, we compare reconstructions obtained from a variety of common illumination patterns qualitatively and quantitatively. We considered illumination patterns where three bright-field measurements are augmented by $(M - 3)$ rings with equal annular radius in the dark-field. Then we fixed the number of illumination patterns to $M = 5$ and 6 and compared our illumination patterns against two designs:

The first design was proposed in [18] in the context of data-driven recovery, where the classic two DPC half-circles in the bright-field are augmented by annular sectors in the dark-field. Unfortunately, in the absence of an additional bright-field measurement we observed the same oriented streaking artifacts as in Fig. 3. Therefore, we use the same three bright-field illumination patterns as for our method and, consequently, partition the dark-field annulus into $(M - 3)$ equisized sectors.

The second design instantiates a random selection similar to the selection proposed by [8] in the original publication on mFPM. There, in each illumination pattern, a fraction of $\frac{1}{M}$ of all LEDs up to ν_{ill} is activated.

We conclude from Fig. 4 ($M = 5$) and Fig. 5 ($M = 6$) that the proposed annular illumination patterns consistently result in superior reconstructions, as seen qualitatively in the Fourier error maps and quantitatively in the SNR and the RMSE. In addition, an increase in the number of measurements from 5 to 6 gives only marginal gains, thus making the pFPM with 5 measurements a fast, practical choice for those applications that necessitate high frame rates.

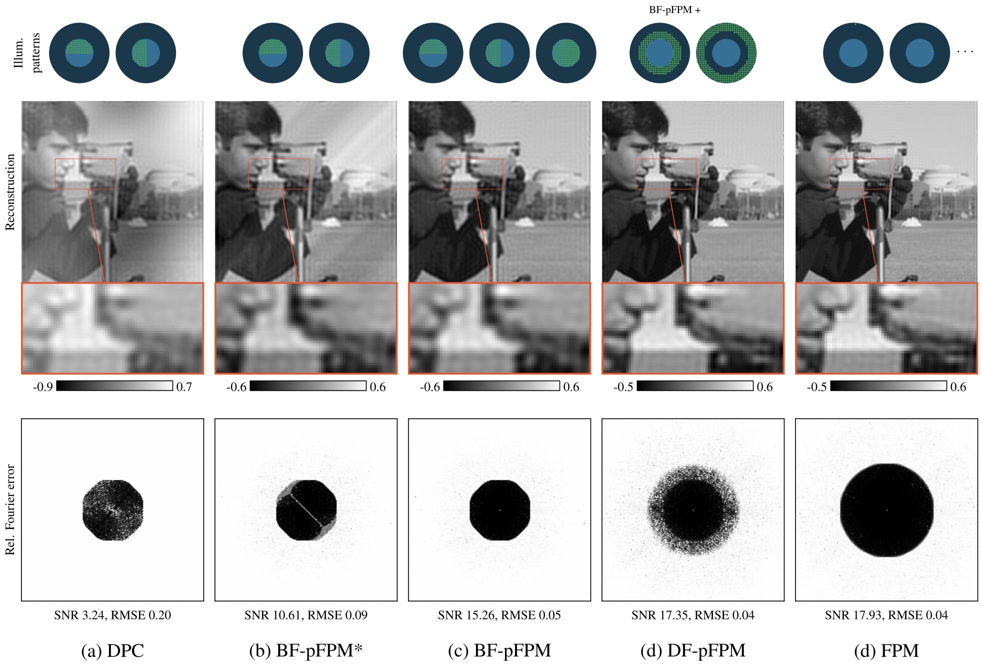

Fig. 3. Simulated measurements. Top to bottom: llumination patterns; phase reconstruction and magnified region in inset; relative Fourier error (14); SNR (15) and RMSE (16) in Fourier space.

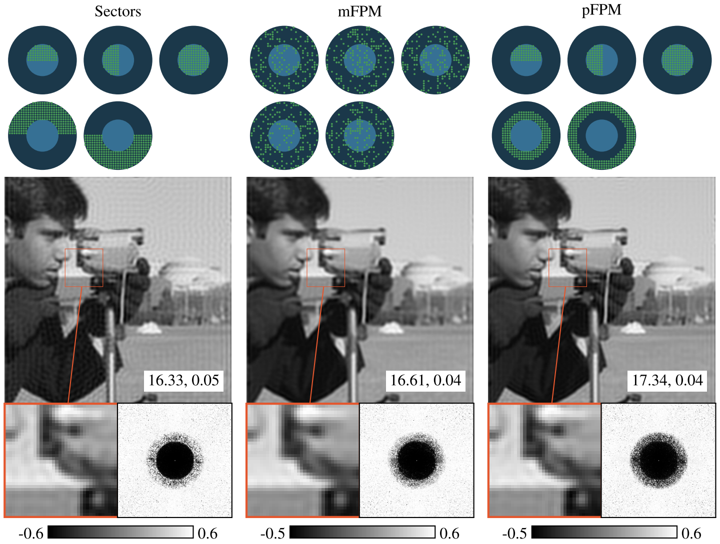

Fig. 4. Reconstructions from different designs of $M = 5$ illumination patterns (left to right: sectors, random, proposed rings). Top: illumination patterns. Middle and inset: reconstruction. Bottom: relative Fourier error map. The numbers in the inset are SNR, NMSE. The colormap applies only to the reconstruction.

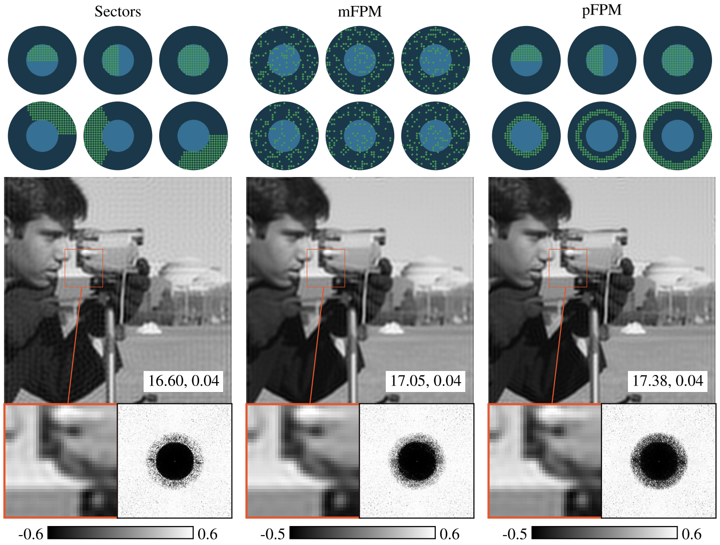

Fig. 5. Reconstructions from different designs of $M = 6$ illumination patterns (left to right: sectors, random, proposed rings). Top: illumination patterns. Middle and inset: reconstruction. Bottom: relative Fourier error map. The numbers in the inset are SNR, NMSE. The colormap applies only to the reconstruction.

4.2. Experimental

We image the USAF-1951 phantom (a phase-only object manufactured by Benchmark Technologies) on a commercial inverted microscope (Nikon TE2000-U). The illumination is provided by a customized quasi-dome LED array (SCI Microscopy) [33] with a central wavelength of 525 nm installed on the location of the transmission illumination unit. The microscope is equipped with a 10× 0.25 NA objective lens (Nikon) and captures intensity measurements with an sCMOS sensor (PCO Edge 5.5 monochromatic) that has a pixel size of 6.5 μm. We use LEDs up to $\nu_{\text{ill}} = 2\nu_{\text{obj}} = 0.5$ for dark-field illumination, which results in a total NA of $\nu_{\text{obj}} + \nu_{\text{ill}} = 0.75$.

The integration time is set to 50 ms for bright-field images and 200 ms ms for dark-field images. This yields a total acquisition time of 550 ms, which could be further reduced by using high-power LEDs or lowering the dynamic range. The important quantity is the number of bright-field and dark-field images, which has been reduced to a minimum in pFPM. Example measurements are shown in Fig. 1 and in Supplement 1.

Like in the simulation results, the DPC reconstruction suffers from low-frequency artifacts, as shown in Fig. 6(a). These are removed by BF-pFPM* at the cost of oriented streaking artifacts, as shown in Fig. 6(b). We conclude from Fig. 6(c) that the additional measurement from full bright-field illumination in BF-pFPM enables satisfactory recovery of all low-frequencies without artifacts. Finally, the addition of two measurements from LEDs in dark-field rings spanning $[1, 1.5]\nu_{\text{obj}}$ and $[1.5, 2]\nu_{\text{obj}}$ enables the recovery of the high-frequency details. This is exemplified with the profile of the fifth element in Group 9 shown in the insets in Fig. 6, which is consistent with the expected resolution of 857 μm and similar to previously-reported resolutions for lower [32] and higher [23] NA. Unlike the reconstructions from the sole bright-field illumination patterns, DF-pFPM clearly resolved this element and hints at the resolution of the sixth element in Group 9, and even of the first element in Group 10. The phase fluctuations around 1 radian also match the target phase difference for this custom resolution target. Finally, the generalization of the L^2 penalty of DPC proves useful, as the DF-pFPM reconstruction is almost free from high-frequency artifacts. A comparison with the reconstructions obtained by using an L^2 penalty and without any penalty is presented in Section 5 of Supplement 1.

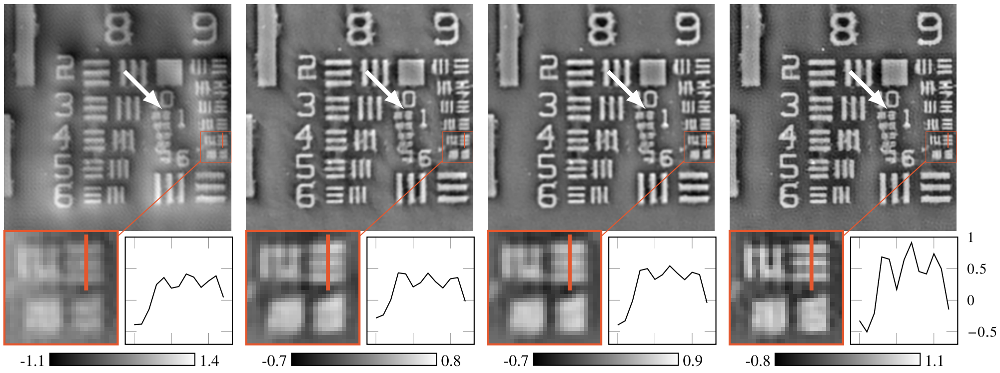

(a) DPC (b) BF-pFPM* (c) BF-pFPM (d) DF-pFPM

Fig. 6. Phase reconstruction from measurements of the USAF-1951 phantom. From top to bottom: phase reconstruction; magnified region in inset around the fifth and sixth element in Group 9 of the phantom and plot of the line profile of the fifth element in Group 9. The axes of the plot are shared between the methods. The white arrow points at the first element in Group 10 that is only resolved with the dark-field information.

The compute cost of the algorithm is determined by the number of proximal Gauss-Newton steps and the number of iterations for the inner solver. For our algorithmic setup, which is discussed in detail in Section 4 of Supplement 1, obtaining the DF-pFPM reconstruction shown in Fig. 6 takes about 35 s on an Apple MacBook Pro equipped with an Apple M3 Max chip. The implementation is entirely matrix-free, which means that we only store images in memory and all operators such as G' in (12) are computed implicitly.

5. Conclusion

We introduce a perturbative approach for phase imaging with a LED-array microscope that enables high-resolution phase imaging with few measurements by combining a perturbative reconstruction algorithm with tailored bright-field and dark-field illumination patterns. The perturbative algorithm, effectively a Gauss-Newton algorithm, is a generalization of the popular DPC to multiple iterations and more sophisticated regularizers with better noise-suppression properties. We demonstrate the feasibility of the approach on simulated as well as on experimental data. The proposed method improves the reconstructions significantly over DPC, at the cost of only two additional measurements from dark-field illumination and without any learned components. The proposed illumination patterns also consistently lead to better reconstructions than other illumination patterns that have been proposed previously. Future work will take advantage of data-driven regularizers to improve reconstructions or decrease exposure time. In addition, we plan to refine the optical models. For instance, the present work did not consider aberrations in the pupil function. Finally, while the current work is dedicated to optical phase imaging with an LED array, it may be extended to X-ray or electron microscopy.

Funding. Schweizerischer Nationalfonds zur Förderung der Wissenschaftlichen Forschung (PZ00P2_216211); Siebel Scholars Foundation; National Science Foundation (DMR 1548924); Chan Zuckerberg Initiative.

Disclosures. The authors declare no conflicts of interest.

Data availability. Data underlying the results presented in this paper are not publicly available at this time but may be obtained from the authors upon reasonable request.

Supplemental document. See Supplement 1 for supporting content.

References

1. F. Zernike, "Phase contrast, a new method for the microscopic observation of transparent objects," Physica **9**(7), 686–698 (1942).
2. Y. Park, C. Depeursinge, and G. Popescu, "Quantitative phase imaging in biomedicine," Nat. Photonics **12**(10), 578–589 (2018).
3. D. Gabor, "A new microscopic principle," Nature **161**(4098), 777–778 (1948).
4. G. Zheng, R. Horstmeyer, and C. Yang, "Wide-field, high-resolution Fourier ptychographic microscopy," Nat. Photonics **7**(9), 739–745 (2013).
5. K. Kim, H. Yoon, M. Diez-Silva, *et al.*, "High-resolution three-dimensional imaging of red blood cells parasitized by *Plasmodium falciparum* and *in situ* hemozoin crystals using optical diffraction tomography," J. Biomed. Opt. **19**(01), 1–011005 (2013).
6. M. Mir, T. Kim, A. Majumder, *et al.*, "Label-free characterization of emerging human neuronal networks," Sci. Rep. **4**(1), 4434 (2014).
7. G. Zheng, C. Kolner, and C. Yang, "Microscopy refocusing and dark-field imaging by using a simple LED array," Opt. Lett. **36**(20), 3987–3989 (2011).
8. L. Tian, X. Li, K. Ramchandran, *et al.*, "Multiplexed coded illumination for Fourier ptychography with an LED array microscope," Biomed. Opt. Express **5**(7), 2376–2389 (2014).
9. L. Tian and L. Waller, "Quantitative differential phase contrast imaging in an LED array microscope," Opt. Express **23**(9), 11394–11403 (2015).
10. G. Zheng, C. Shen, S. Jiang, *et al.*, "Concept, implementations and applications of Fourier ptychography," Nat. Rev. Phys. **3**(3), 207–223 (2021).
11. C. Zheng, W. Wang, Y. Ji, *et al.*, "High-space–bandwidth product characterization of metalenses by information fusion of multi-angle illumination," Optica **12**(3), 374–383 (2025).
12. L.-H. Yeh, J. Dong, J. Zhong, *et al.*, "Experimental robustness of Fourier ptychography phase retrieval algorithms," Opt. Express **23**(26), 33214–33240 (2015).
13. J. Dong, L. Valzania, A. Maillard, *et al.*, "Phase retrieval: From computational imaging to machine learning: A tutorial," IEEE Signal Process. Mag. **40**(1), 45–57 (2023).
14. D. Hamilton and C. Sheppard, "Differential phase contrast in scanning optical microscopy," J. Microsc. **133**(1), 27–39 (1984).
15. S. B. Mehta and C. J. Sheppard, "Quantitative phase-gradient imaging at high resolution with asymmetric illumination-based differential phase contrast," Opt. Lett. **34**(13), 1924–1926 (2009).
16. J. Sun, C. Zuo, J. Zhang, *et al.*, "High-speed fourier ptychographic microscopy based on programmable annular illuminations," Sci. Rep. **8**(1), 7669 (2018).
17. M. Kellman, E. Bostan, M. Chen, *et al.*, "Data-driven design for Fourier ptychographic microscopy," in *International Conference on Computational Photography* (IEEE, 2019), pp. 1–8.
18. Y. Xue, S. Cheng, Y. Li, *et al.*, "Reliable deep-learning-based phase imaging with uncertainty quantification," Optica **6**(5), 618–629 (2019).
19. P. Bohra, T. A. Pham, Y. Long, *et al.*, "Dynamic Fourier ptychography with deep spatiotemporal priors," Inverse Problems **39**(6), 064005 (2023).
20. B. Lee, J. Y. Hong, D. Yoo, *et al.*, "Single-shot phase retrieval via fourier ptychographic microscopy," Optica **5**(8), 976–983 (2018).
21. X. He, C. Liu, and J. Zhu, "Single-shot fourier ptychography based on diffractive beam splitting," Opt. Lett. **43**(2), 214–217 (2018).
22. J. Sun, Q. Chen, J. Zhang, *et al.*, "Single-shot quantitative phase microscopy based on color-multiplexed fourier ptychography," Opt. Lett. **43**(14), 3365–3368 (2018).
23. C. Zheng, S. Zhang, S. Liu, *et al.*, "Single-shot fourier ptychographic microscopy with isotropic lateral resolution via polarization-multiplexed led illumination," Biomed. Opt. Express **15**(2), 672–686 (2024).
24. H. Yoon, H. Chae, K. C. Lee, *et al.*, "Single-shot fourier ptychography using polarization-encoded illumination," Appl. Phys. Lett. **126**(12), 123702 (2025).
25. R. Wang, L. Yang, Y. Lee, *et al.*, "Spatially-coded fourier ptychography: flexible and detachable coded thin films for quantitative phase imaging with uniform phase transfer characteristics," Adv. Opt. Mater. **12**(15), 2303028 (2024).
26. J. Sun, Q. Chen, Y. Zhang, *et al.*, "Sampling criteria for fourier ptychographic microscopy in object space and frequency space," Opt. Express **24**(14), 15765–15781 (2016).
27. J. Zhang, T. Xu, Z. Shen, *et al.*, "Fourier ptychographic microscopy reconstruction with multiscale deep residual network," Opt. Express **27**(6), 8612–8625 (2019).
28. H. Wang, J. Zhu, Y. Li, *et al.*, "Neuph: Scalable and generalizable neural phase retrieval with local conditional neural fields," Adv. Photon. Nexus **3**(05), 056005 (2024).
29. L. Tian, Z. Liu, L.-H. Yeh, *et al.*, "Computational illumination for high-speed in vitro Fourier ptychographic microscopy," Optica **2**(10), 904–911 (2015).
30. M. R. Kellman, E. Bostan, N. A. Repina, *et al.*, "Physics-based learned design: Optimized coded-illumination for quantitative phase imaging," IEEE Trans. Comput. Imaging **5**(3), 344–353 (2019).

31. S. Salzo and S. Villa, “Convergence analysis of a proximal Gauss-Newton method,” Comput Optim Appl **53**(2), 557–589 (2012).
32. R. Wu, Z. Luo, M. Liu, *et al.*, “Fast fourier ptychographic quantitative phase microscopy for in vitro label-free imaging,” Biomed. Opt. Express **15**(1), 95–113 (2024).
33. Z. F. Phillips, R. Eckert, and L. Waller, “Quasi-dome: A self-calibrated high-NA LED illuminator for Fourier ptychography,” in *Imaging Systems and Applications* (2017), paper IW4E-5.
34. M. Zach, K.-C. Shen, R. Cao, *et al.*, “perturbative-fpm,” GitHub (2022), https://github.com/Biomedical-Imaging-Group/perturbative-fpm.